MAVIS: System modelling and performance prediction

Guido Agapito[a,c], Daniele Vassallo[b,c], Cedric Plantet[a,c], Valentina Viotto[b,c], Enrico Pinna[a,c], Benoit Neichel[d], Thierry Fusco[d], and Francois Rigaut[e]

[a]INAF Osservatorio Astrofisico di Arcetri, L. Enrico Fermi 5, 50125 Firenze, Italy
[b]INAF Osservatorio Astronomico di Padova, Vicolo dell'Osservatorio 5, 35122, Padova, Italy
[c]ADaptive Optics National laboratory in Italy (ADONI)
[d]Laboratoire d'Astrophysique de Marseille, 38 Rue Frédéric Joliot Curie, 13013 Marseille, France
[e]AAO - Stromlo, RSAA, Australian National University, Cotter Road, Weston, ACT2600, Australia

ABSTRACT

The MCAO Assisted Visible Imager and Spectrograph (MAVIS) Adaptive Optics Module has very demanding goals to support science in the optical: providing 15% SR in V band on a large FoV of 30arcsec diameter in standard atmospheric conditions at Paranal. It will be able to work in closed loop on up to three natural guide stars down to H=19, providing a sky coverage larger than 50% in the south galactic pole. Such goals and the exploration of a large MCAO system parameters space have required a combination of analytical and end-to-end simulations to assess performance, sky coverage and drive the design. In this work we report baseline performance, statistical sky coverage and parameters sensitivity analysis done in the phase-A instrument study.

Keywords: Adaptive Optics, Wave-front Sensing, Numerical Simulation, Multi-conjugate adaptive optics, Tomographic Reconstruction, AO performance, AO for the optical, High angular resolution

1. INTRODUCTION

Numerical simulations have been used to support system design in selecting the baseline configuration of the AO module of MAVIS[1] with main focus on the fulfilment of the Top Level Requirements (TLRs). These requirements demand that the system reaches 10% SR in V band on a FoV of 30arcsec diameter (15% goal) in standard atmospheric conditions at Paranal with bright Natural Guide Stars (m_J=8) and provides a sky coverage larger than 50% in the south galactic pole guaranteeing an ensquared energy of at least 15% on 50mas side in V band (in the same standard atmospheric conditions).

Most of the work has been done through, in particular, sensitivity analysis to different parameters, error terms, with a few different tools. These tools that have also been used to compute synthetic PSFs to support the design of the MAVIS imager and spectrograph modules,[2,3] are presented in the next section, 2. Then, the article continues with the description of the parameters of the baseline configuration of the MAVIS AO module[4] in Sec. 3, its error budget in Sec. 4, and, finally, in Sec. 5, we briefly describe the sensitivity analyses done.

2. SIMULATION TOOLS

To evaluate MAVIS AO module performance and to perform a comprehensive sensitivity analysis we used two main tools: the end-to-end INAF's AO simulations tool PASSATA[5] and a faster, Fourier-based tool, which is mostly based on the article by Neichel et al. 2009.[6] In this section we focus on a few important features of both of them.

The PASSATA simulates all the processes that take place during the operation of an AO system, from input disturbance generation and propagation down to wavefront correction via the deformable mirrors (DMs). Control implemented in end-to-end simulations is described in Ref. 7 and it is based on tomographic reconstruction and DM projection,[8] pseudo-open loop control (POLC)[9] and split tomography.[10]

In the next sub-sections we examine a few aspects of the simulation tools that may interest the reader: the generalized fitting error that is used to optimize the altitude and the pitch of the post focal DMs, the LGS sodium elongation that is required to account for the truncation effects and for the correct noise in the LGS sub-apertures, and the sky coverage estimation that is fundamental for the estimation of the statistics of the performance of the system.

2.1 Generalized fitting

Once we have the tomographic reconstruction of the turbulence, we need to apply a correction with the DMs. This is done by minimizing the difference between the projection of the phase from the reconstructed layers and the projection of the phase from the DMs. The error coming from this is called generalized fitting and it is studied to optimize the altitude and the pitch of the DMs.

We use a specific tool based on the approach described in Ref. 11. Thanks to its low computation power requirements it is useful to evaluate a large combination of parameters as shown in Sec. 5. We cross-checked the results of this tool with both PASSATA and Fourier* and we got good agreement.

2.2 LGS sodium elongation

PASSATA computes the LGS spot for each sub-aperture as a convolution of the PSF of a point source affected by the residual turbulence in conic propagation and the extended spots given by the laser geometry. The LGS spots modelling takes into account the broadening effect due to upward propagation (FWHM=1.2 arcsec), the geometry of the Shack-Hartmann WFS, of the launcher and of the sodium profile. This convolution is done at high resolution with elements size of $0.5\lambda_{\mathrm{LGS}}/d_{\mathrm{sub-ap}}$. and then the correct sampling of the detector is obtained with a down-scaling of the arrays.

2.3 Sky coverage

While the high-order (modes above tip/tilt) residuals can be assessed independently from the observed FoV, the jitter residual has to be computed statistically, assuming a certain distribution of the stars. The sky coverage analysis is mainly performed with a code developed at Laboratoire d'Astrophysique de Marseille (LAM), with some cross-checks with a similar code developed at INAF/Arcetri. The pipeline consists of the following steps:

- **Asterism catalog generation.** The source we use for stars statistics is the Besançon galaxy model.[12] We get from the model a list of stars in a $3° \times 3°$ field at the South Galactic Pole. These stars are placed with a uniform probability. We then generate a series of pointing coordinates and we register all 3-star asterisms at each pointing. Fields with only 1 or 2 stars are also registered.

- **Low-order residual computation.** For each registered asterism, we compute the LO residual (tip/tilt) in a given direction as follows:
$$\sigma_{LO} = \sqrt{\sigma_{vib}^2 + \sigma_{tomo}^2 + \sigma_{noise}^2} \qquad (1)$$
where σ_{vib}^2 is the tip/tilt Mean Square Error (MSE) due to vibrations (computed with formulas from Ref. 13), σ_{tomo}^2 is the pure tomographic error[14] and σ_{noise}^2 is the WFS noise term.

- **Jitter in the scientific FoV**. We compute the jitter in 5 directions in the scientific FoV: on axis and on 4 positions, close to the corners of the imager FoV, at 20" off axis. The average jitter in the FoV is simply found by averaging these 5 residuals.

---

*in these cases we compute generalized fitting error as the difference between a simulation with the actual DMs and one with a large number of DMs (equal to the number of reconstructed layers).

- **Sky coverage computation**. The selected asterism for each pointing is the one giving the lowest average jitter in the scientific FoV. We then compute the sky coverage as the ratio between the number of fields giving a jitter less or equal to a given value and the total number of fields:

$$SC(x) = \frac{\sum_i P_i(\text{Jitter} \leq x)}{N_{\text{fields}}} \tag{2}$$

with $P_i(\text{Jitter} \leq x) = 1$ if the i-th field has an asterism giving a jitter less than x and $P_i(\text{Jitter} \leq x) = 0$ otherwise.

3. BASELINE CONFIGURATION

In this section we report the parameters used in the baseline configuration. They are summarized in Tab. 1. This configuration was chosen not only considering simulations results coming from the work reported here, but also considering all the aspects of the design of MAVIS.[1,4] In Sec. 5 some of these parameters were changed to explore all the selected different configurations. For example, for the study of the optimal LGS asterism with Fourier-based tool we used a set of Stereo-SCIDAR Cn^2 profiles.[15] In this baseline configuration we consider the pseudo open loop control with split tomography as described in Ref. 7, but other simulation work focused on predictive control and learn and apply approach in the context of the AO module of MAVIS is reported in Ref. 16 and 17 respectively. This baseline configuration gives an average residual error over the science FoV of 125nm that is less than the 132nm of the requirement (that corresponds to 10% SR in V band).

As an example, a couple of V band PSFs from end-to-end simulations are shown in Fig. 1.
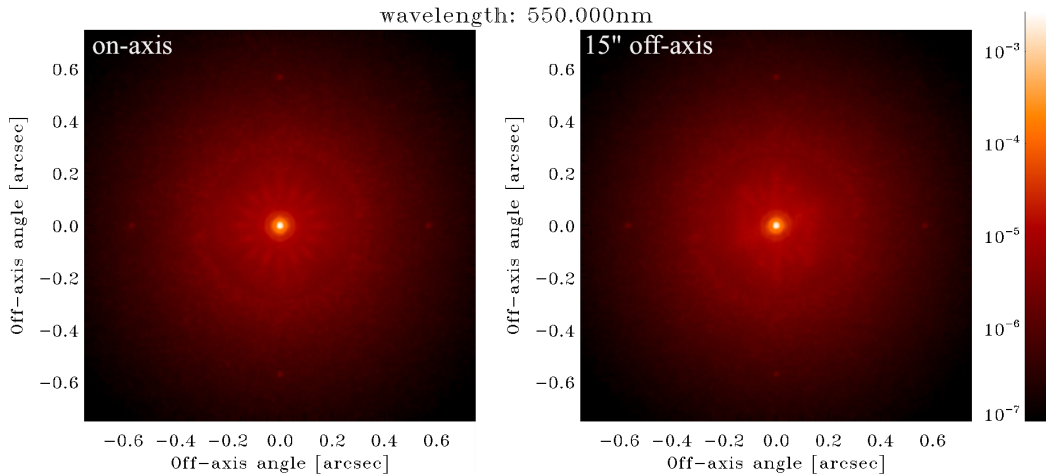

FIGURE 1: V band PSFs for the baseline configuration from an end-to-end simulation: left, on-axis one, right, 15arcsec off-axis one.

4. ERROR BUDGET

We present in Table 2 the residual WFE breakdown from end-to-end simulations in the baseline configuration for both high and low orders. We quantified each error source individually. The sum of individual HO terms (∼91 nm, summing up generalized fitting, tomographic, measurement noise, temporal and aliasing errors) is in good agreement with the HO residual of an end-to-end simulation in which all these error sources are included (∼92 nm). The difference is +14 nm and could be due to the assumptions used to compute the error terms individually. In particular, it is difficult to fully isolate each of them and the computation assumes that they are independent, which is not exactly the case. This argument can explain why the root sum square of all individual terms is different than the end-to-end simulation result. Finally, we are assuming bright NGSs (m_J=8) for low orders sensing. In medium flux regime (m_J=15), ∼25 nm of measurement noise error have to be added.

TABLE 1: Summary of the baseline MAVIS parameters (in simulation).

Parameter	value
Telescope diameter	8m
Central obstruction	1.28m
Pupil mask	round, no spiders
Zenith angle	30deg
Science FoV (diameter)	30
Technical FoV (diameter)	120
Atmospheric turbulence	1 profile with 10 layers (Paranal median)
r_0	0.126m
L_0	25m
NGS full throughput	0.28
LGS full throughput (with laser splitting)	0.184
Ground DM	conjugated at 0m with ∼0.22m pitch
Post focal DM no 1	conjugated at 6000m with ∼0.25m pitch
Post focal DM no 2	conjugated at 13500m with ∼0.32m pitch
NGS WFS number	3
NGS WFS off-axis angle (good asterism)	20 arcsec
NGS WFS nSA	1
NGS WFS FoV	3 arcsec
NGS WFS pixel pitch	30 mas
NGS WFS detector RON	0.5 e^-/pixel/frame
NGS WFS detector dark current	20 e^-/pixel/s
NGS (H band) sky background	2100 e^-/m^2/arcsec^2/s (no moon)
NGS flux (full aperture, good asterism)	1000 ph/ms
LGS WFS number	8
LGS WFS off-axis angle	17.5 arcsec
LGS WFS nSA	40x40
NGS WFS FoV	5.0 arcsec
LGS WFS pixel pitch	0.866 mas
LGS WFS detector RON	0.2 e^-/pixel/frame
LGS launcher number	4
LGS launcher off-axis distance	5.5 m
LGS flux per sub-aperture (0.04 m^2)	75 ph/ms
Sodium profile	"multi peak"[18]
Control	POLC with split tomography[7]
Reconstruction layers altitude	[0, 0.33, 0.65, 1.25, 2.50, 5.00, 8.75, 12.50, 16.25] km
Reconstruction layers pitch	[0.20, 0.20, 0.20, 0.20, 0.20, 0.22, 0.26, 0.30, 0.35] m
Centroiding algorithm	CoG (LGS), weighted CoG (NGS)
Framerate	1000Hz
Total delay	2ms
Integrator gains	0.3-0.4 (LGS), 0.5 (NGS)
Extra error term	28nm[4]

Note: NGS is Natural Guide Star, LGS is Laser Guide Star, DM is Deformable Mirror, WFS is Wavefront Sensor,
SA is Sub-Aperture, FoV is Field of View, RON is Read-Out Noise, POLC is pseudo-open loop control and
CoG is Center of Gravity.

5. SENSITIVITY ANALYSIS

Asterism   As a preliminary step, we explored the system sensitivity to the geometry of the LGS asterism, both in terms of number of stars and asterism radius. Since we included generalized fitting error in these simulations, we also considered DM pitches as a third parameter to explore. The purpose of this analysis is to make a first guess of the most interesting system configurations and to start constricting the parameter space. As it concerns the DM pitches, not all the values we explored are even practically feasible.

TABLE 2: Breakdown of MAVIS AO residual wavefront error.

High Orders

Error term	Error [nm]
High-frequency fitting error	65.3
Generalized fitting error	30.1
Tomographic error	47.6
Measurement noise error	40.6
Temporal error	34.7
Aliasing error	40.1
Sodium elongation/truncation	23.6
LGS jitter	6.1

Low Orders

Error term	Error [nm]
Tomographic error	38.0
Measurement noise error	~ 0
Temporal error	29.2
Wind shake/vibrations	5.5

For each combination of the three parameters, we computed with Fourier the overall contribution of tomographic, full fitting (generalized+high-frequency) and noise errors, averaged over MAVIS field of view and over 243 Stereo-SCIDAR profiles[15] corresponding to median seeing conditions (0.7" @z=30°). Results are reported in Table 3.

TABLE 3: Residual wavefront error with Fourier (limited to tomographic, fitting and noise error) for several combinations of number of guide stars, asterism radius and DM pitches.

Asterism radius [arcsec]	DM pitches [cm]	Residual [nm]		
		4 LGS	6 LGS	8 LGS
17.5	(30,40)	111	98	96
17.5	(30,30,40)	103	87	85
17.5	(20,20,20)	94	75	71
25.0	(30,40)	128	104	100
25.0	(30,30,40)	122	95	90
25.0	(20,20,20)	115	85	78
30.0	(30,40)	140	110	103
30.0	(30,30,40)	135	102	94
30.0	(20,20,20)	130	93	84

One of the most interesting comparisons among the ones explored with Fourier is between 4 and 8 LGSs for the smallest asterism radius. We ran end-to-end simulations over these two configurations with the baseline configuration (see Tab.1) and we found that only 8 LGSs are able to meet the requirement of 10% SR in V-band with the ESO-TLR atmospheric profile (Figure 2). It is also important to point out that performance from these end-to-end simulations cannot be directly compared with Fourier because we are using different Cn^2 profiles and, moreover, our Fourier simulations only account for a few error terms (tomographic, fitting and noise) out of the whole budget.

Generalized fitting We calculated the generalized fitting error for several altitudes of the post-focal DMs using Fourier. The analysis shows that good ranges are 5-7km and 13-15km (figure 3).

Number of sub-apertures We report in Table 4 the results of the sensitivity analysis on the number of sub-apertures of the LGS WFSs. In this analysis (performed with PASSATA) we also explored three different LGS flux levels. Noise covariance used to compute the tomographic reconstructor has been optimized iteratively for each combination of the two parameters. We found very similar results for the 36×36 and 40×40 cases in the flux regime we are mainly interested in. Further simulation work is needed in the next phase to validate these preliminary conclusions.
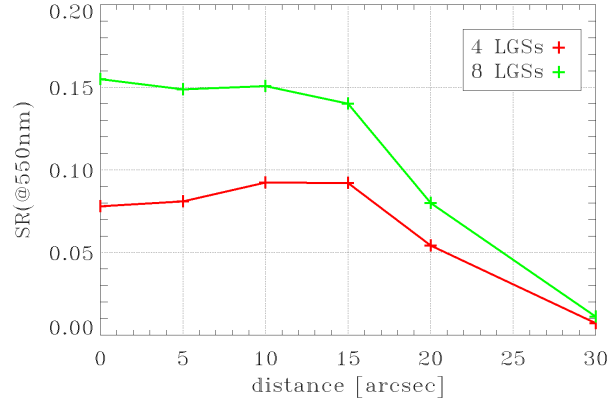
FIGURE 2: V-band SR (from end-to-end) versus off-axis angle for 4 and 8 LGSs, 17.5" radius and baseline configuration (see Tab.1).
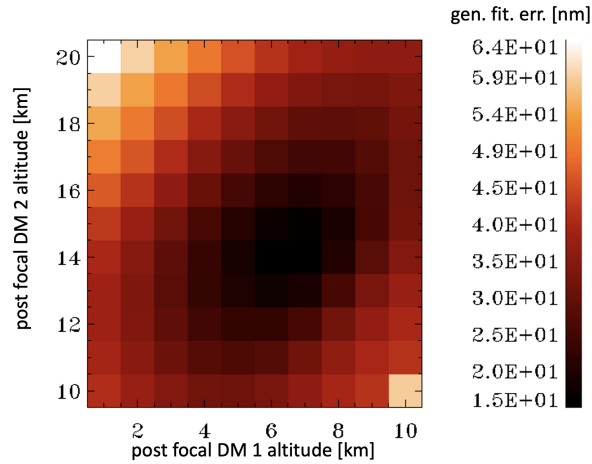

FIGURE 3: Generalized fitting error (with Fourier) as a function of the altitude of post-focal DMs.

TABLE 4: Relative on-axis residual wavefront error in nm (with PASSATA) as a function of the number of sub-apertures (Nsa) of the LGS WFSs and of the LGS flux (in ph/ms/subap on a 40×40 WFS). The reference configuration has a 0 relative error.

Nsa / Flux	32	36	40
37.5	+43.4	+37.3	+40.1
75	+17.8	-6.0	0
150	-24.1	-29.1	-29.6

Temporal error We ran LGSs-only simulations in PASSATA to quantify the sensitivity to average wind speed and AO loop delay. Results are reported in Table 5.

Temporal control filters We analysed the possibility to use higher order filters (infinite impulse response one) instead of pure integrators to better shape closed loop transfer functions and improve performance thanks to a better rejection of temporal and noise errors, in particular with lower fluxes. We have limited our analysis to the HO/LGSs control, but it could be extended to LO/NGSs too. The optimization of this filter for a system with pseudo open loop control is not trivial because POLC introduces a multi-input multi-output dynamic control term given by the matrix H described in Ref. 7. Currently, we have no way to consider this term in the control filter optimization, and, so, we are limited to optimization tools designed for single conjugate AO systems.[19,20] Our approach has been a trial-and-error one, where we optimize filters with different turbulence

TABLE 5: Relative on-axis residual wavefront error in nm (with PASSATA) as a function of AO loop delay (in frames) and average wind speed (in m/s). The reference configuration has a 0 relative error.

delay \ wind speed	1.0	5.1	10.2	20.4
2.0	-36.4	-31.9	0	+67.6
2.5	-34.6	-29.5	+17.2	+73.5
3.0	-19.4	-0.5	+36.7	+88.0

parameters and noise level and we run end-to-end simulation to evaluate their performance. A comparison between integrator and the optimized filters based controller is presented in Fig.4. In particular, these filters are able to improve performance in low flux regime: considering a sodium return flux of 0.4e7 ph/s/m^2 (corresponding to 28 ph/ms/sa) the improvement is larger than 3% V band SR with respect to a pure integrator controller, and gets very close to the same performance (difference is ∼1% V band SR) of a pure integrator with a higher return flux of 1.07e7 ph/s/m^2 (75 ph/ms/sa). But even in the highest flux condition considered, 75 ph/ms/sa, they lead to an improvement of ∼ 3% V band SR.
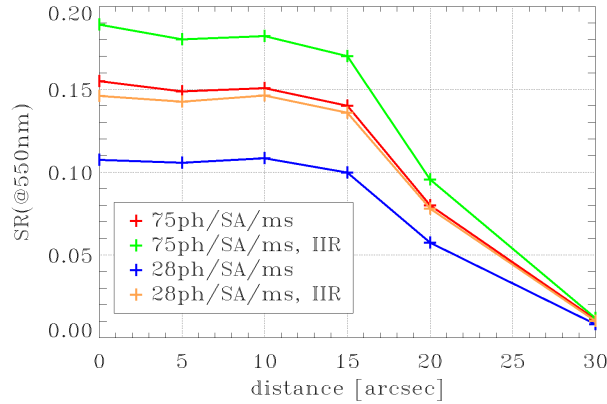

FIGURE 4: V-band SR (from end-to-end) in function of off-axis angle for standard flux condition and 90% flux condition with integrator and infinite impulse response (IIR) filters (optimized as show in Sec.5) controllers.

Seeing For this analysis, we ran a batch of end-to-end simulations changing the seeing parameter while keeping the same normalized Cn^2 profile. For simplicity, we ran simulations with LGSs only, so LGSs are used to measure tip/tilt too. Results show that residual variance follows approximately a $(r_{0a}/r_{0b})^{5/3}$ law. This is expected since, as can be seen in Ref. 21, fitting error and Shack-Hartmann WFS aliasing error follow a $(d/r_0)^{5/3}$ law and fitting error is the largest term in our AO error budget.

Spot elongation The LGS spot in a given sub-aperture is characterized by an elongation and orientation that both depend on the position of the sub-aperture itself with respect to the launcher. A possible configuration to maximize the available WFS FoV (that is square) is to rotate the WFS such that the most elongated spots fall on the diagonal of the sub-aperture (the 45° configuration, hereafter). This is important because truncated spots (i.e. spots that are not fully imagined in the sub-apertures FoV) give a not null signal even with a flat wavefront.

We ran a batch of simulations considering two different sodium profiles and two WFS orientations. Sodium profiles are the "multi-peak" and "very wide" ones from Ref. 18, which are fairly representative of a "good" and a "bad" case, respectively. WFS orientations are 0° (non-optimized) and 45° (optimized). Results are reported in Table 6.

Na profile FoV	Very Wide		Multi-Peak	
conf. angle [deg]	0	45	0	45
Science (r≤15")	36	30	25	24
Technical (15"<r≤60")	62	54	38	38

Cn^2 update Tomographic reconstruction requires knowledge of the turbulence statistics. In simulations (both PASSATA and Fourier) we can use our direct knowledge of the input 3D atmospheric disturbance to build a "perfect" turbulence covariance matrix. If the Cn^2 profile varies during the night, the reconstructor should in principle be updated, otherwise performance might be affected. To investigate this effect, we selected 4 consecutive stereo-SCIDAR profiles[15] (spanning half an hour in total) and we linearly interpolated them to get a time resolution of 20 seconds. For each time point we ran the Fourier code to compute the residual wavefront error, both with and without updating the reconstructor. Results are shown in Figure 5. The loss in performance without the update is stable after 10 minutes between 10 and 15nm. We also ran end-to-end simulations in the same conditions and we found a good agreement with Fourier results.
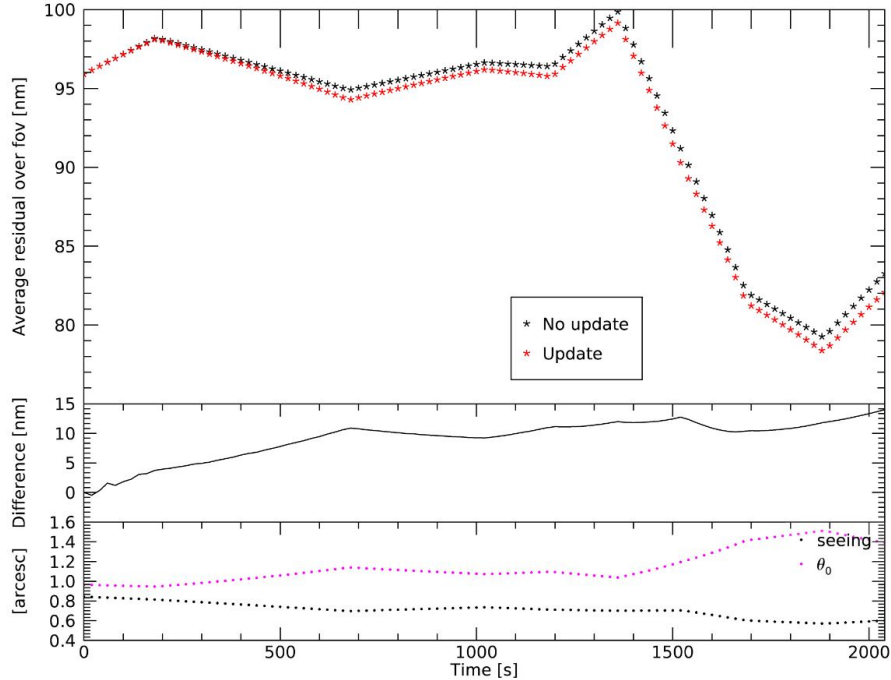

FIGURE 5: Top panel: absolute residual wavefront error with Fourier (averaged over the FoV) as a function of time, with and without updating the tomographic reconstructor. Middle panel: the difference between the two curves. Bottom panel: temporal trends of seeing and θ_0.

5.1 Sky coverage

Here we report the sensitivity analysis on Low Orders, i.e. on the correction given by the NGSs on tip/tilt and quadratic term of plate scale. The residual of this correction -the residual jitter- depends on the NGS asterism we have for a given observation. Following step-by-step the procedure outlined in Section 2.3.

Asterism catalog generation. The statistics of the available stars in the technical FoV is plotted in Figure 6. No star of magnitude H ≤ 20 is available in about 5% of the cases, while only one H ≤ 20 star is available

in 15% of the cases, excluding the possibility to correct quadratic plate scale modes. Then, the number of available H ≤ 20 stars is less than 3 in 35% of the case. Finally, a star of magnitude H ≤ 16 is available in 50% of the cases, providing enough flux to get one tip/tilt measurement at a high frame rate (for effective wind shake/vibrations compensation).
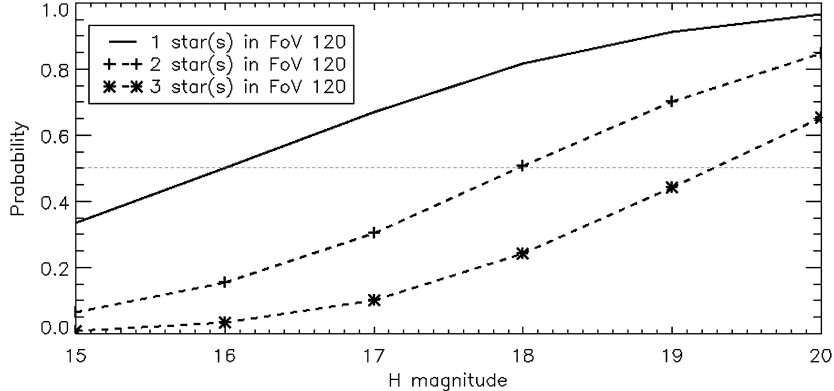

FIGURE 6: Probability of finding 1, 2 or 3 stars in MAVIS technical FoV when pointing towards the South Galactic Pole.

Low-order residual computation. As detailed in Section 2.3, the three dominant contributors to the overall residual jitter are temporal error, noise and tomographic error. The first is mostly dominated by windshake residuals and only depends on the NGS loop frequency. The residual vs framerate is plotted in Figure 7(a), for a global jitter that comprises both windshake/vibrations and atmosphere. Noise jitter versus flux is plotted in 7(b). We assumed for this calculation a 50% SR, a noise level on the detector of 1 e- RMS, an overall transmission of 0.25 for the NGS WFSs and a bandpass including both H and J bands. In these conditions, a H=16 magnitude star would give ∼50 photons/frame/VLT pupil (at 500Hz). The conversion from photons to noise is based on noise propagation computations.

Finally, Figure 8 shows the tomographic error (on-axis) for an equilateral constellation of 3 stars. The absolute amount of jitter due to tomography depends on the Cn^2 profile and the outer scale of the turbulence.

Sky coverage computation. In Table 7 we summarize the expected jitter for different sky coverage percentages at two galactic altitudes. The sky coverage curves are shown in Fig. 9. We add the 2×2 sub-apertures case to check the impact on jitter of having three of such sensors that are able to measure tip/tilt and give the truth sensing on focus and astigmatisms. The main conclusion is that for 50% Sky Coverage at the pole, we should expect a jitter of about 25mas.

TABLE 7: Expected jitter at South Pole and 30° galactic altitude as a function of sky coverage.

Sky Coverage	jitter [mas]	
	Pole	30°
20%	16.5	10
50%	25	15
70%	30	18

6. CONCLUSION AND FUTURE WORK

MAVIS design is still in the preliminary phase, but we already have a set of tools for system modelling and performance prediction. We have shown how we verified that the baseline configuration is able to guarantee the fulfilment of the TLRs.
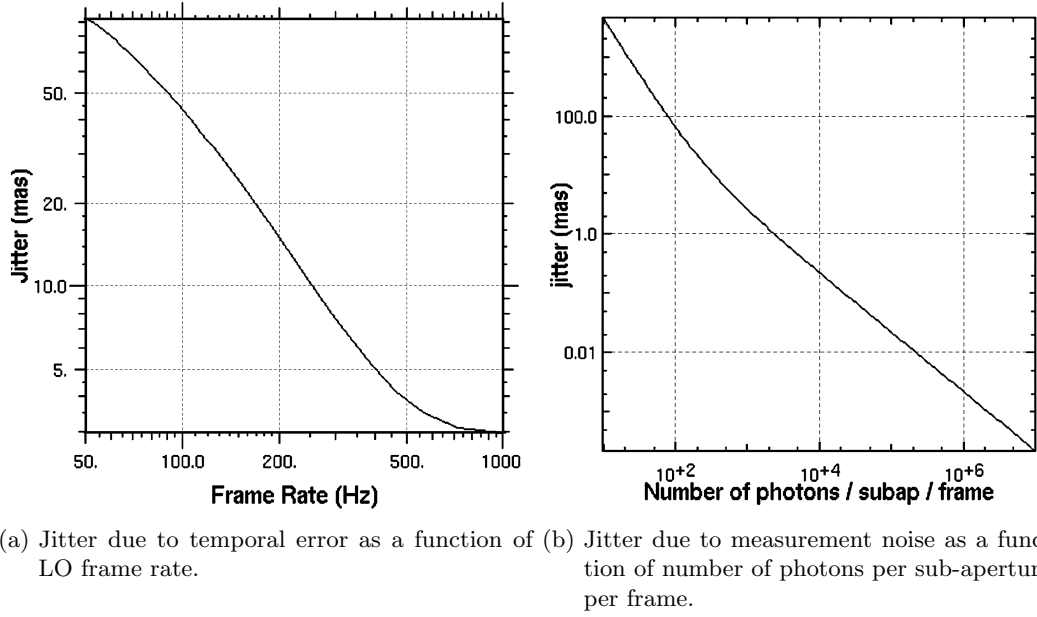
(a) Jitter due to temporal error as a function of LO frame rate.

(b) Jitter due to measurement noise as a function of number of photons per sub-aperture per frame.
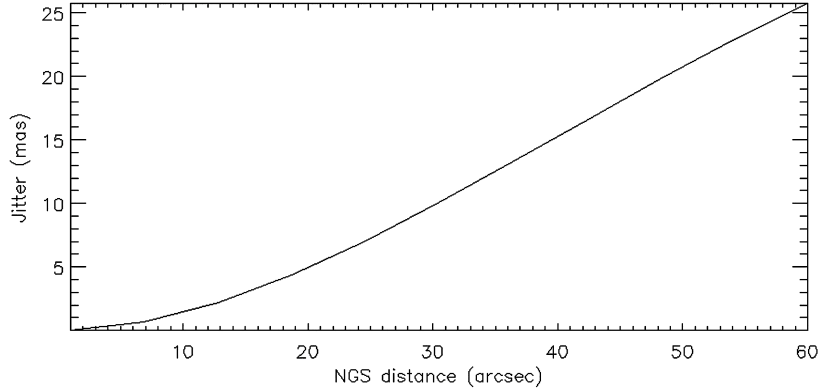
FIGURE 7: Jitter error in mas.

FIGURE 8: "Tomographic" Jitter (on-axis) as a function of the distance from the center.

In the next design phase we will progress in the sensitivity study analysis and update the performance prediction with a more accurate model of the system (for example considering the influence functions of the deformable secondary mirror of the VLT[22] and the telescope spiders). Moreover, we will revise our control scheme in coordination with the real time computer team[23] to improve the final performance to be more robust to some critical aspect such sodium return flux.

REFERENCES

[1] Rigaut, F. et al., "MAVIS conceptual design," **11447**, in these proceedings.

[2] Ellis, S. et al., "MAVIS: science case, imager, and spectrograph," **11447**, in these proceedings.

[3] Monty, S. et al., "The MAVIS Image Simulator: predicting the astrometric performance and sensitivity of MAVIS," **11447**, in these proceedings.

[4] Viotto, V. et al., "MAVIS: The Adaptive Optics Module feasibility study," **11448**, in these proceedings.

[5] Agapito, G., Puglisi, A., and Esposito, S., "PASSATA: object oriented numerical simulation software for adaptive optics," *Proc. SPIE* **9909**, 99097E–99097E–9 (2016).

[6] Neichel, B., Fusco, T., and Conan, J.-M., "Tomographic reconstruction for wide-field adaptive optics systems: Fourier domain analysis and fundamental limitations," *JOSA A* **26**(1), 219–235 (2009).
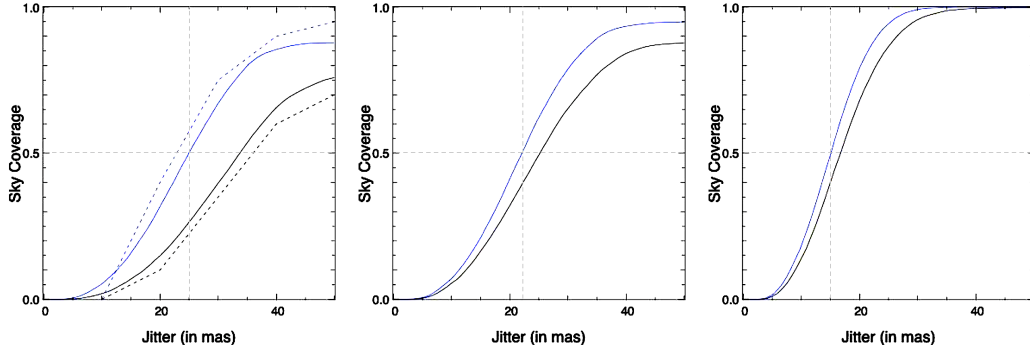
FIGURE 9: Sky coverage: left, for the galactic pole, middle, 60degrees above the galactic plane and, right, 30 degrees above the plane. Blue lines are for a 1×1 WFS and black lines are for a 2×2 WFS. For the galactic pole, the dashed plots are the results when using the Arcetri simulation tool.

[7] Busoni, L., Agapito, G., Plantet, C., Oberti, S., Verinaud, C., Le Louarn, M., Esposito, S., and P., C., "Adaptive optics design status of MAORY, the MCAO system of european ELT," in [*Adaptive Optics for Extremely Large Telescopes 6 - Conference Proceedings*], (2019).

[8] Fusco, T., Conan, J.-M., Rousset, G., Mugnier, L. M., and Michau, V., "Optimal wave-front reconstruction strategies for multiconjugate adaptive optics," *J. Opt. Soc. Am. A* **18**, 2527–2538 (Oct 2001).

[9] Ellerbroek, B. L. and Vogel, C. R., "Simulations of closed-loop wavefront reconstruction for multiconjugate adaptive optics on giant telescopes," in [*Astronomical Adaptive Optics Systems and Applications*], Tyson, R. K. and Lloyd-Hart, M., eds., *Proc. SPIE* **5169**, 206 – 217 (2003).

[10] Gilles, L. and Ellerbroek, B. L., "Split atmospheric tomography using laser and natural guide stars," *J. Opt. Soc. Am. A* **25**, 2427–2435 (Oct 2008).

[11] Rigaut, F. J., Ellerbroek, B. L., Flicker, R., and Wizinowich, P. L., "Principles, limitations, and performance of multiconjugate adaptive optics," **4007**, 1022–1031 (07 2000).

[12] Robin, A. and Creze, M., "Stellar populations in the milky way: a synthetic model.," **157**, 71–90 (Mar. 1986).

[13] Correia, C. M., Neichel, B., Conan, J.-M., Petit, C., Sauvage, J.-F., Fusco, T., Vernet, J. D. R., and Thatte, N., "Natural guide-star processing for wide-field laser-assisted AO systems," in [*Adaptive Optics Systems V*], Marchetti, E., Close, L. M., and Véran, J.-P., eds., **9909**, 1301 – 1313, International Society for Optics and Photonics, SPIE (2016).

[14] Sasiela, R. J., "Wave-front correction by one or more synthetic beacons," *J. Opt. Soc. Am. A* **11**, 379–393 (Jan 1994).

[15] Osborn, J., Wilson, R. W., Sarazin, M., Butterley, T., Chacón, A., Derie, F., Farley, O. J. D., Haubois, X., Laidlaw, D., LeLouarn, M., Masciadri, E., Milli, J., Navarrete, J., and Townson, M. J., "Optical turbulence profiling with Stereo-SCIDAR for VLT and ELT," *Monthly Notices of the Royal Astronomical Society* **478**, 825–834 (04 2018).

[16] Cranney, J., Zhang, H., Doucet, N., Rigaut, F., Gratadour, D., De Doná, J., Hong, Y., Ltaief, H., and Keyes, D., "Predictive Learn and Apply: MAVIS application - Apply," **11448**, in these proceedings.

[17] Zhang, H., Cranney, J., Doucet, N., Hong, Y., Gratadour, D., Ltaief, H., Keyes, D., and Rigaut, F., "Predictive Learn and Apply: MAVIS application - Learn," **11448**, in these proceedings.

[18] Pfrommer, T. and Hickson, P., "High resolution mesospheric sodium properties for adaptive optics applications," **565**, A102 (May 2014).

[19] Agapito, G., Arcidiacono, C., Quiros-Pacheco, F., Puglisi, A., and Esposito, S., "Infinite impulse response modal filtering in visible adaptive optics," in [*Adaptive Optics Systems III*], Ellerbroek, B. L., Marchetti, E., and Veran, J.-P., eds., **8447**, 1071 – 1080, International Society for Optics and Photonics, SPIE (2012).

[20] Agapito, G. and Pinna, E., "Semianalytical error budget for adaptive optics systems with pyramid wave-front sensors," *Journal of Astronomical Telescopes, Instruments, and Systems* **5**(4), 1 – 8 (2019).

[21] Rigaut, F. J., Veran, J.-P., and Lai, O., "Analytical model for Shack-Hartmann-based adaptive optics systems," in [*Adaptive Optical System Technologies*], Bonaccini, D. and Tyson, R. K., eds., *Proc. SPIE* **3353**, 1038 – 1048 (1998).

[22] Briguglio, R., Biasi, R., Xompero, M., Riccardi, A., Andrighettoni, M., Pescoller, D., Angerer, G., Gallieni, D., Vernet, E., Kolb, J., Arsenault, R., and Madec, P.-Y., "The deformable secondary mirror of VLT: final electro-mechanical and optical acceptance test results," in [*Adaptive Optics Systems IV*], Marchetti, E., Close, L. M., and Véran, J.-P., eds., **9148**, 1403 – 1410, International Society for Optics and Photonics, SPIE (2014).

[23] Gratadour, D. et al., "MAVIS Real-Time Control system," **11448**, in these proceedings.